energies

MDPI

Article

Photovoltaic Energy Storage System Based on Bidirectional LLC Resonant Converter Control Technology

Di Xie [1], Liangliang Wang [2,*], Zhi Zhang [3], Shoumo Wang [2], Longyun Kang [1] and Jigang Yao [2]

[1] New Energy Research Center, School of Electric Power, South China University of Technology, Guangzhou 510640, China
[2] Guangdong HYNN Technologies Co., Ltd., Dongguan 523808, China
[3] Department of Electrical Engineering and Automation, Dongguan University of Technology, Dongguan 523808, China
* Correspondence: wanglljx@foxmail.com

Abstract: Bidirectional DC/DC converters are widely adopted in new energy power generation systems. Because of the low conversion efficiency and non-isolation for conventional, bidirectional DC/DC converters in the photovoltaic energy storage complementary system, this paper proposes a bidirectional isolation LLC converter topology, with compensating inductance for the energy storage system; it has excellent characteristics, such as wide input voltage range and soft switching in full-load range. First, an AC equivalent model based on the fundamental wave equivalent method is established to derive the voltage gain. Meanwhile, a small signal model is also built to design a reasonably closed-looped controller. Finally, the improved bidirectional LLC resonant converter is applied to the photovoltaic energy storage complementary system. The correctness and feasibility for the bidirectional LLC converter topology under the proposed charging and discharging control strategy of the DC bus are verified by simulation and experimental results.

Keywords: photovoltaic; energy storage; LLC; bidirectional DC/DC converter

Citation: Xie, D.; Wang, L.; Zhang, Z.; Wang, S.; Kang, L.; Yao, J. Photovoltaic Energy Storage System Based on Bidirectional LLC Resonant Converter Control Technology. *Energies* **2022**, *15*, 6436. https://doi.org/10.3390/en15176436

Academic Editor: Hongwen He

Received: 1 August 2022
Accepted: 30 August 2022
Published: 3 September 2022

1. Introduction

In recent years, global energy shortages and environmental degradation have led to the rapid development of renewable energy power-generation technology. However, due to the intermittency of renewable energy, some serious problems, including poor stability, reliability, and power quality, are produced in the power system, so an energy storage system must be equipped to solve the problems above [1,2].

In the household photovoltaic system, energy storage devices are added to improve the scheduling and control of the system energy and optimize the energy utilization rate of the system. The photovoltaic and energy storage systems, with similar topological structures, are commonly called photovoltaic energy storage complementary systems. A single-phase, two-stage photovoltaic energy storage complementary system is shown in Figure 1, where the system consists of solar panels, boost converters, bidirectional DC/DC converters, battery packs, inverters, relays, etc. There are two significant features in the system. On the one hand, PV panels provide renewable energy for the energy storage complementary system via the boost converter. On the other hand, under the conditions set by the system for the charging and discharging of the battery [3–5], the inverter will feed the excess energy to the load or the grid, which plays the role of the peak modulation.

Moreover, the bidirectional DC/DC converter is adopted as the energy storage conversion module in the photovoltaic energy storage complementary system; it has the feature of bidirectional power flow and plays the role of regulating power, recovering energy, and maintaining the stability of the power supply. Usually, bidirectional DC/DC converters are divided into the non-isolated type and the isolated type [6–9]. Non-isolated conventional, bidirectional, buck–boost converters are used as the bidirectional DC/DC converters, which

have the characteristics of low costs and simple control strategies. However, there are also obvious disadvantages, including narrow voltage range and low conversion efficiency in the non-isolated buck–boost converters. In addition, the ripples of the direct component and the alternating component are not effectively filtered, which could affect the life of lithium batteries.

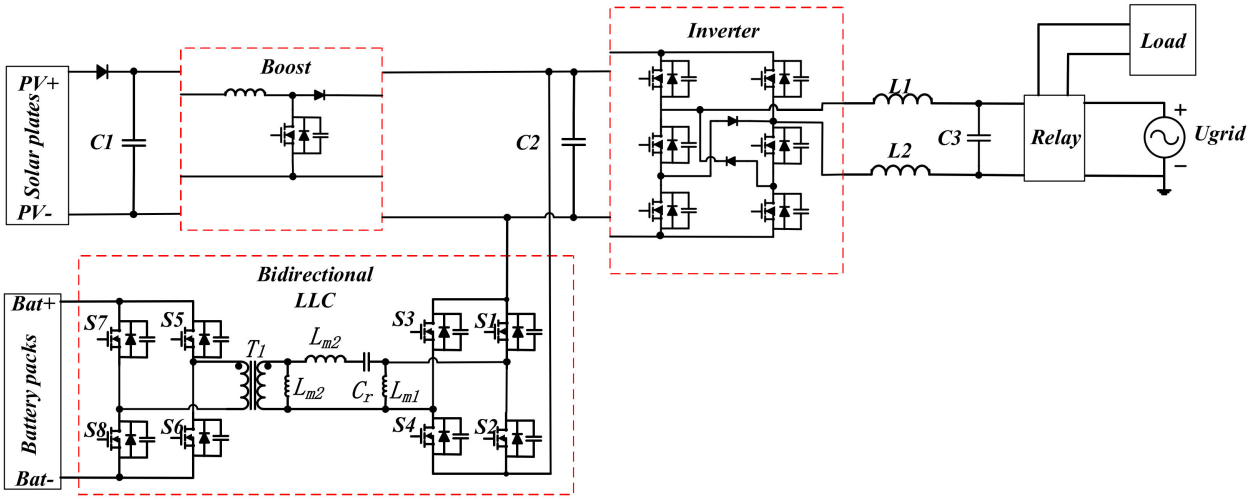

Figure 1. Structure of photovoltaic energy storage complementary system.

Isolated converters are utilized to effectively solve problems in non-isolated converters. A bidirectional series resonant DC/DC converter topology with an isolated topology structure is proposed [10], where a zero-current-switching (ZCS) turn-off for diodes can be achieved. Therefore, problems such as circulating energy and turn-off loss can be completely solved, but the converter can only operate in the step-down mode due to the peak value of 1 for voltage gain. Compared with the bidirectional series resonant DC/DC converters, bidirectional LLC resonant converters can achieve zero-voltage-switching (ZVS) turn-on of power switching and ZCS turn-off of diodes, and it has the following features: higher conversion efficiency and wider range of voltage gain. A bidirectional LLC resonant converter with a conventional topology structure realizes bidirectional power conversion by replacing the rectifier diodes with power switches in the single-phase LLC circuit. However, the efficiency of the converter is seriously affected due to the problems composed of narrow soft-switching range, large turn-off current, and large circulating energy.

In order to improve the efficiency of the traditional LLC resonant converter, other methods are used, e.g., optimal control strategy [11,12], optimal efficiency design [13,14], and peak gain method [15,16]. However, the topological structure and control scheme of the above schemes are complicated, and the operation characteristics, such as wide voltage range, wide frequency range, and high conversion efficiency cannot be achieved at the same time.

For the problems above, a bidirectional LLC resonant converter with compensating inductance is proposed; it not only retains the excellent characteristics of wide input voltage range and soft switching for the conventional, single-phase LLC resonant converter under full load range, but also has the advantages of high conversion efficiency and an isolated topology structure. The symmetry of the converter topology structure can be achieved due to the addition of the compensating inductance. Moreover, it has the feature of simple control, and soft-switching characteristics can be achieved in both directions of power flow.

In this paper, the operation principle of the LLC bidirectional DC/DC converter is analyzed. An AC equivalent model is established by the basic wave equivalent method for the analysis of voltage gain. Then, a small signal model is built to design a reasonable closed-loop controller based on the actual application. Last but not least, the paper discusses the system bus control strategy for the charging and discharging mode. Experiment

results on the photovoltaic energy storage complementary system verified that there is higher conversion efficiency and higher stability in the system schemes compared to the conventional schemes.

2. Operation Principle of Bidirectional LLC Resonant Converter

The bidirectional LLC resonant converter has excellent advantages in soft-switching characteristics, high power conversion efficiency, frequency modulation, voltage modulation characteristics, and low switching loss. The resonant converter can also operate in a state where the output voltage gain is less than 1, which is often used in an operational state, where the output voltage gain is greater than 1. When it operates at a voltage gain less than 1, the operation principle of the bidirectional LLC resonant converter is similar to that of a series resonant converter [17–20]. The topology of the bidirectional LLC resonant converter is shown in Figure 2.

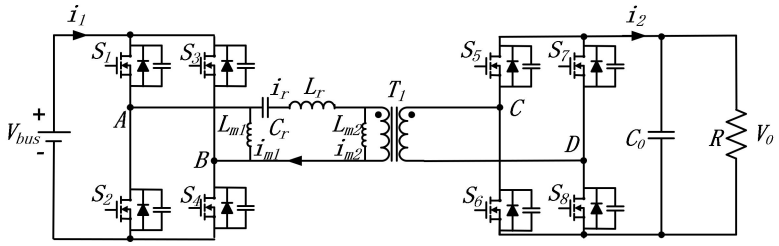

Figure 2. Bidirectional LLC resonant converter.

The primary side of the converter is the high-voltage side of the bus, and the secondary side is low-voltage side. There are full-bridge circuits on both the primary and secondary sides of the transformer. MOSFET was selected as the switch. *Vbus* represents the power supply voltage on the high-voltage side, and *i1*, *Co*, *R*, *i2*, and *Vo* denote the input current, capacitance of the low-voltage output side, load, output current, and output voltage of the battery storage system. The resonant inductor *Lr* is in series with the resonant capacitor *Cr* in the series resonant circuit, the turn ratio of the transformer *T1* is N: 1, and the output port of the full bridge on the high-voltage side is parallel with a compensation inductor Lm1. The resonant frequency is obtained by

$$f_r = \frac{1}{2\pi\sqrt{L_r C_r}} \tag{1}$$

To simplify the analysis, the following assumptions are made: (1) All switches, diodes, inductors, and capacitors are ideal components, and the capacitances of all MOSFET parasitic capacitors are equal; (2) ignore transformer leakage inductance and any parasitic resistances. Ideally, the transformer is equivalent to an inductor, with an inductance equal to the magnetizing inductance on the input side.

When energy flows from the high-voltage side to the low-voltage side, it is defined as positive flow; otherwise, it is defined as negative flow. Meanwhile, the voltage gain is defined as

$$\mathrm{G} = \frac{\mathrm{n}V_o}{V_{bus}} \tag{2}$$

According to the circuit analysis, when the energy flows in the negative direction, the role of the compensating inductor *Lm1* is equivalent to that of the magnetizing inductor *Lm2*, while the energy flows in the positive direction. Therefore, the topological structure after voltage conversion is symmetric, which indicates that there is consistency in both the analyses of the energy positive flow process and negative flow process. Therefore, the positive flow process of the energy is selected for analysis in detail.

The bidirectional LLC resonant converter realizes the function of adjusting the output voltage through the variable frequency control method [21–23]. On the rated state, the

operation mode of the converter is mainly divided into the following three kinds: switching frequency is lower than the resonant frequency, switching frequency is equal to the resonant frequency, and switching frequency is greater than the resonant frequency.

Combined with the three operation states, the following control strategies are designed: (1) When fs is less than fr, as shown in Figure 3, the driving signals of the upper and lower switch on the primary side of the transformer *T1* are complementary, which means that the driving signals of *S1* and *S4*, and *S2* and *S3* are synchronized; the secondary side of transformer adopts the synchronous rectifier control method. When the current in the switch drops to 0, the driving signal synchronizes to 0. When the current in the diode of another switch body appears in the same bridge arm, the switch is immediately turned on. (2) When fs is greater or equal to fr, the control on the primary is consistent with the operation state above; the driving signals of the switches on the secondary side are the same as on the corresponding positions of the primary side.

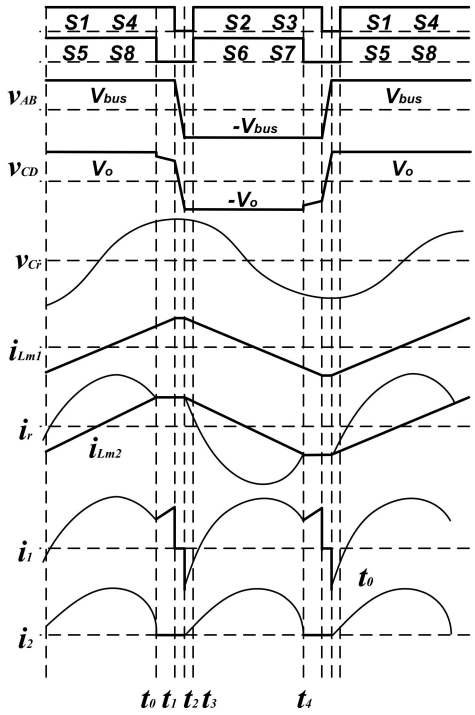

Figure 3. The theoretical waveform at switching frequency below the resonant frequency.

Because the analysis methods of (1) and (2) are similar, and the energy storage system mostly operates in (1) under charging and discharging models, the operation state of (1) is analyzed in detail.

There is no DC component in the LLC resonant circuit of the full-bridge topology, which determines that the operating principles are symmetric during the front and latter half periods, so their analysis methods are similar. As shown in Figure 3, the operation state during the latter half cycle can be divided into four stages:

Interval 1 (*t0* to *t1*): A series resonant loop consists of *Lr*, *Cr*, and *Lm2*, and the resonant current *ir* is equal to the magnetizing current *iLm2*. The voltage *VLm2* on the magnetizing inductor and the resonant frequency $fr1$ can be given by

$$\begin{cases} -nV_o < v_{Lm2}(t_0) < nV_o \\ v_{Lm2}(t_0) = \frac{k}{1+k}(V_{bus} - v_{Cr}(t_0)) \end{cases} \tag{3}$$

$$f_{r1} = \frac{1}{2\pi\sqrt{(L_{m2} + L_r)C_r}} \tag{4}$$

This stage starts when switches *S1* and *S4* are turned on; *VAB* is equal to *Vbus*; *Lr*, *Cr*, and *Lm2* start resonating; voltage *VCr* across the resonant capacitor *Cr* rises continuously, and current *iLm1* of the compensation inductor rises. Since *Lm2* > *Lr*, *fr1* < *fr*. When operating at full load, the curves of *ir* and *iLm2* are approximately horizontal during the interval from *t0* to *t1*, as shown in Figure 3.

Interval 2 (*t1* to *t2*): This interval starts when switches *S1* and *S4* are turned off, as shown in Figure 4b. At the time, the bus voltage *Vbus* charges the parasitic capacitors of switches *S1* and *S4*, and the parasitic capacitors of switches *S2* and *S3* discharge.

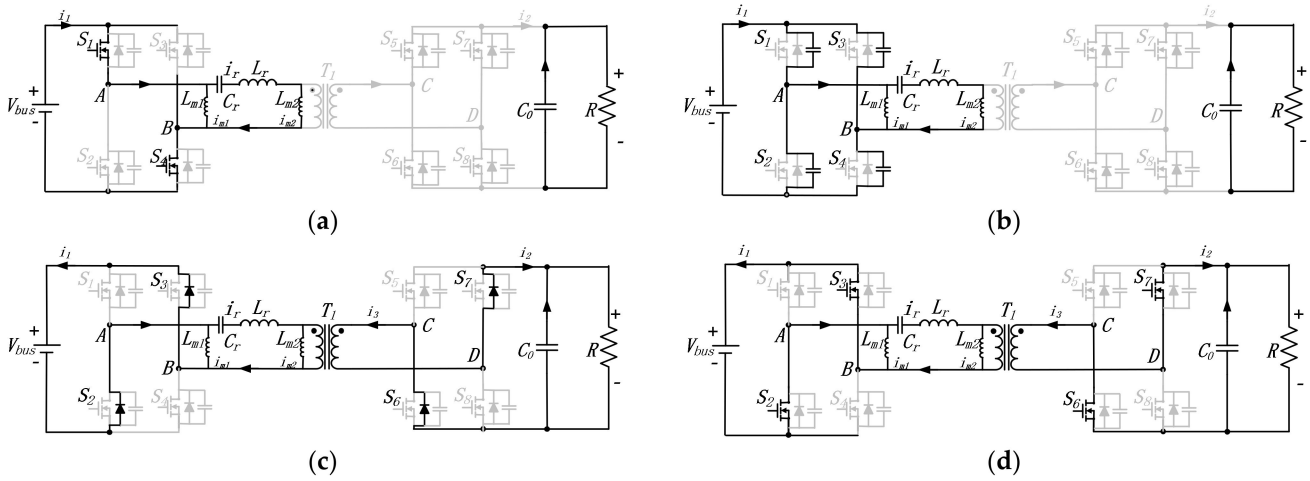

Figure 4. Equivalent circuit for different modes under below-resonance operation, and (**a**–**d**) show the corresponding circuit operating interval 1 to 4, respectively.

VAB drops rapidly, and voltage *VLm2* on the magnetic inductance also changes rapidly. When (5) is satisfied, the body diodes of switches *S6* and *S7* conduct naturally, and *VLm2* is clamped to $-Vo$. Because values of the parasitic capacitances are very small, the time is very short from *t1* to *t2*; there is no change for *iLm1*, *iLm2*, *ir*, and *VCr* during this interval. Voltage *VLm2* on the magnetic inductance can be determined by

$$v_{Lm2}(t) = -\frac{k}{1+k}(V_{bus} + v_{Cr}(t)) < -nV_o \tag{5}$$

Interval 3 (*t2* to *t3*): This interval starts when the parasitic capacitors of *S2* and *S3* begin discharging. When the parasitic capacitors of *S2* and *S3* discharge fully, *VAB* is clamped to -*Vbus*, and i1 flows through the body diodes of the *S2* and *S3* to realize the zero-voltage switching (ZVS) turn-on of switches *S2* and *S3*.

The resonant frequency fr of the circuit is shown in (1). *iLm1*, *iLm2*, and *ir* begin to decrease, and the resonant current *ir* is less than theb magnetizing current *iLm2*. Because ir is greater than 0, *VCr* continues to rise. Until *ir* is less than 0, *VCr* begins to decrease.

Interval 4 (*t3* to *t4*): At *t3*, the bidirectional LLC resonant converter achieves the ZVS turn-on of *S2* and *S3*. Similar to the operation principle of *S2* and *S3*, the ZVS turn-on of the switch can also be achieved for *S6* and *S7*. When *VAB* is equal to -*Vbus*, *VAB* is clamped, and -*Vo*, *iLm1*, and *iLm2* decrease. When *ir* is equal to 0, the *VCr* reaches the peak. When *ir* is less than 0, *VCr* goes down.

3. Characteristics Analysis of Bidirectional LLC Resonant Converter

With the operation principle, the wide range of voltage regulation characteristics and soft-switched characteristics [24,25] of the LLC resonant converter are analyzed in detail. As the main component of the voltage and current parameters were sinusoidal in the resonant tank, the basic wave-equivalent analysis method was utilized in the DC voltage gain analysis.

3.1. Analysis of Voltage Gain

As can be seen in Figure 2, the converter was divided into three parts: full-bridge inverter module, full-bridge rectifier module, and resonant network. The model was built based on the fundamental wave-equivalent analysis method. The full-bridge inverter module is equivalent to an AC voltage source. The AC voltage source is given by

$$v_i = \frac{4V_{bus}\sin\omega t}{\pi} \tag{6}$$

The control strategy of the full-bridge rectifier module is a synchronous rectifier, and the secondary side of the resonant converter can be equivalent to an AC equivalent load. The AC equivalent load is given by

$$R_{eq} = \frac{n^2 v_{eq}}{i_{eq}} = \frac{8n^2 R_o}{\pi^2} \tag{7}$$

According to (6) and (7), the resonant converter can be equivalent to a linear network. An AC equivalent circuit diagram of the bidirectional LLC resonant converter is shown in Figure 5.

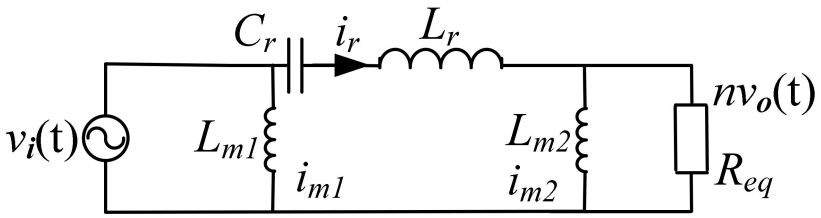

Figure 5. AC equivalent circuit of bidirectional LLC resonant converter.

Assume that the AC gain for the AC equivalent circuit of the bidirectional LLC resonant converter is g, which is defined, as follows:

$$g = nv_{eq}/v_i \tag{8}$$

By analyzing the AC equivalent circuit in Figure 5, the AC gain in the frequency domain can be obtained as

$$g(j\omega_s) = \frac{j\omega_s L_{m2} \;||\; R_{eq}}{1/j\omega_s C_r + j\omega_s L_r + j\omega_s L_{m2} \;||\; R_{eq}} \tag{9}$$

fn is defined as the ratio of fs to fr. The impedance Zr and quality factor Q of the resonant network are given by, respectively,

$$\begin{cases} Z_r = \sqrt{L_r/C_r} \\ Q = Z_r/R_{eq} \\ f_n = f_s/f_r = \omega_s\sqrt{(L_{m2}+L_r)C_r} \end{cases} \tag{10}$$

According to the fundamental equivalence analysis method, it is known that the DC gain g of the bidirectional LLC resonant converter was approximately equal to the AC gain g in the AC equivalent circuit. By applying (10) to (9), the DC voltage gain can be described as

$$\begin{aligned} \mathrm{G} &\approx |g| \\ &= \frac{1}{\sqrt{\left[1+\frac{L_r}{L_{m2}}\left(1-\frac{1}{f_n^2}\right)\right]^2 + Q^2\left(f_n-\frac{1}{f_n}\right)^2}} \end{aligned} \tag{11}$$

Based on the fundamental wave-equivalence method, the voltage gain curve [26,27] is shown in Figure 6, when the converter operated at full load. According to (11), it can be

seen that the voltage gain curve changed smoothly. In other words, when the switching frequency range from 50 kHz to 160 kHz is designed by this method, the voltage gain range from 1.3 to 0.8 can be obtained, which can meet the actual voltage fluctuation demand and has a sufficient margin for the system.

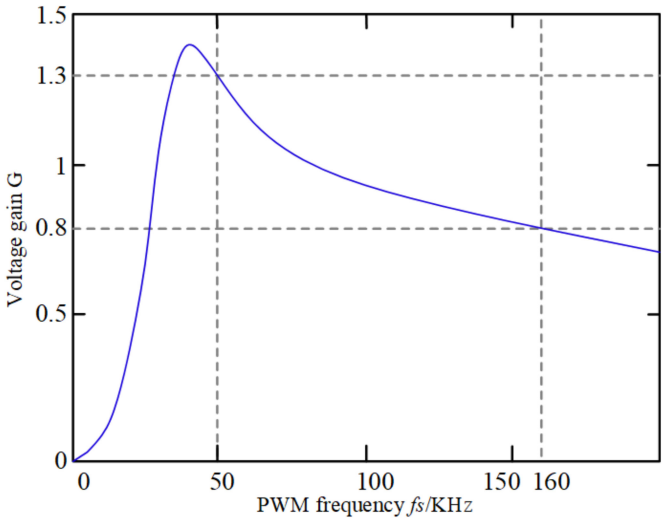

Figure 6. Fundamental equivalent method voltage gain curve.

3.2. Small Signal Analysis

The bidirectional LLC resonant converter consisted of a full-bridge inverter module, resonant circuit, and full-bridge rectifier module. The mathematical model of a bidirectional LLC resonant converter was established by the envelopment analysis method [28–31]. Furthermore, a small-signal model of the bidirectional LLC resonant converter could be obtained, as shown in Figure 7.

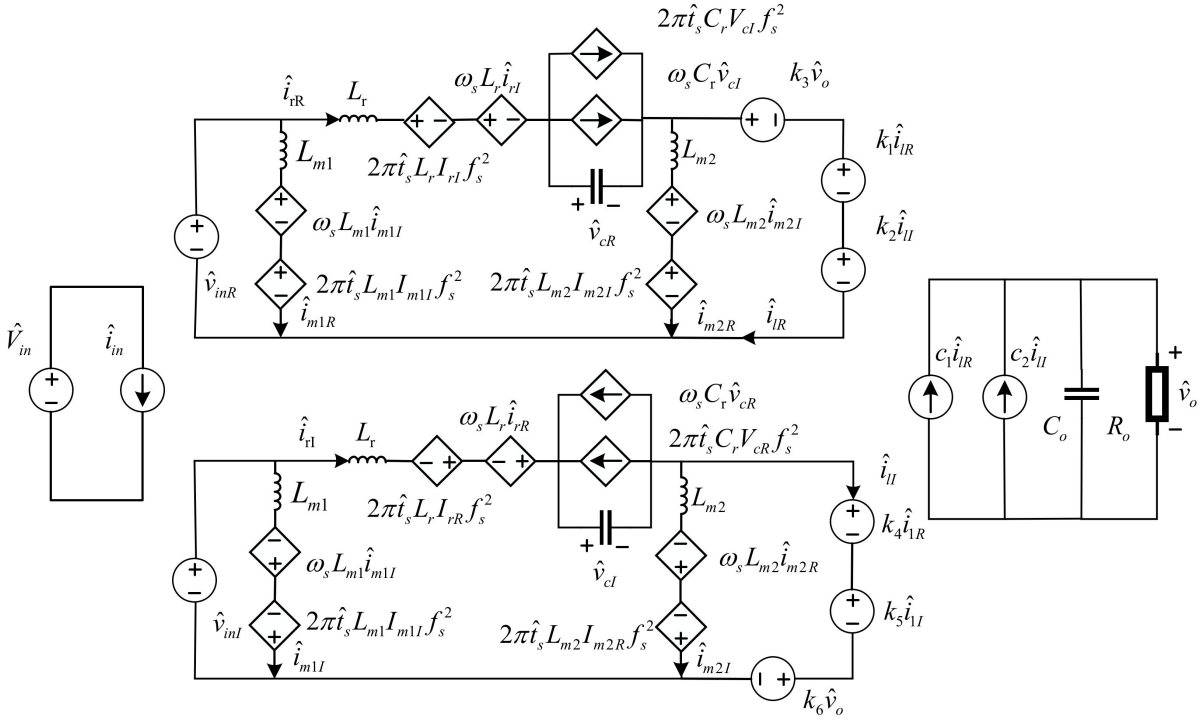

Figure 7. Small signal model of bidirectional LLC resonant converter.

According to Figure 7, the circuit equations of the rectifier module small-signal model are shown in Equation (12),

$$\begin{cases} \hat{i}_o = c_1\hat{i}_{lR} + c_2\hat{i}_{lI} \\ \hat{v}_{lR} = k_1\hat{i}_{lR} + k_2\hat{i}_{lI} + k_3\hat{v}_o = 4n\hat{v}_o\hat{i}_{lR}/\pi\hat{i}_l \\ \hat{v}_{lI} = k_4\hat{i}_{lR} + k_5\hat{i}_{lI} + k_6\hat{v}_o = 4n\hat{v}_o\hat{i}_{lI}/\pi\hat{i} \end{cases} \tag{12}$$

where, *k1*, *k2*, *k3*, *k4*, *k5*, *k6*, *c1*, and *c2* are defined as follows:

$$k_1 = \frac{4n\hat{i}_{lI}^2\hat{v}_o}{\pi\sqrt{\left(\hat{i}_{lI}^2+\hat{i}_{lR}^2\right)^3}}, k_2 = -\frac{4n\hat{i}_{lI}\hat{i}_{lR}\hat{v}_o}{\pi\sqrt{\left(\hat{i}_{lI}^2+\hat{i}_{lR}^2\right)^3}}, k_3 = \frac{4n\hat{i}_{lR}}{\pi\sqrt{\hat{i}_{lI}^2+\hat{i}_{lR}^2}}, k_4 = k_2, k_5 = \frac{4n\hat{i}_{lR}^2\hat{v}_o}{\pi\sqrt{\left(\hat{i}_{lI}^2+\hat{i}_{lR}^2\right)^3}},$$
$$k_6 = -\frac{4n\hat{i}_{lI}}{\pi\sqrt{\hat{i}_{lI}^2+\hat{i}_{lR}^2}}, c_1 = \frac{2n\hat{i}_{lR}}{\pi\sqrt{\hat{i}_{lI}^2+\hat{i}_{lR}^2}} \text{ and } c_2 = \frac{2n\hat{i}_{lI}}{\pi\sqrt{\hat{i}_{lI}^2+\hat{i}_{lR}^2}}$$

According to Figure 7, the circuit equations of the small-signal model of the two-way LLC resonant converter, with the addition of compensating inductance, can be obtained, as shown in (13).

Based on the small signal model, the state space average method was adopted to establish the transfer function of the system, and the matrix equations were established by (12), where *A*, *B*, *C*, and *D* are the coefficient matrixes of the state equation, *x* is the vector composed of various state variables, x' is the first derivative of vector *x*, *u* is the input vector, and *y* is the output vector.

$$\begin{cases} L_r\left(\frac{d\hat{i}_{rI}}{dt} - \omega_s\hat{i}_{rR} - 2\pi f_s^2\hat{t}_s I_{rR}\right) + \hat{v}_{cI} + \hat{v}_{lI} = \frac{4\hat{v}_{in}}{\pi} \\ L_r\left(\frac{d\hat{i}_{rR}}{dt} + \omega_s\hat{i}_{rI} + 2\pi f_s^2\hat{t}_s I_{rI}\right) + \hat{v}_{cR} + \hat{v}_{lR} = 0 \\ C_r\left(\frac{d\hat{v}_{cI}}{dt} - \omega_s\hat{v}_{cR} - 2\pi f_s^2\hat{t}_s C_r V_{cR}\right) = \hat{i}_{rI} \\ C_r\left(\frac{d\hat{v}_{cR}}{dt} + \omega_s\hat{v}_{cI} + 2\pi f_s^2\hat{t}_s C_r V_{cI}\right) = \hat{i}_{rR} \\ L_{m2}\left(\frac{d\hat{i}_{m2I}}{dt} - \omega_s\hat{i}_{m2R} - 2\pi f_s^2\hat{t}_s I_{m2R}\right) = \hat{v}_{lI} \\ L_{m2}\left(\frac{d\hat{i}_{m2R}}{dt} + \omega_s\hat{i}_{m2I} + 2\pi f_s^2\hat{t}_s I_{m2I}\right) = \hat{v}_{lR} \\ C_o\frac{d\hat{v}_o}{dt} + \frac{\hat{v}_o}{R_o} = \frac{2n}{\pi}\hat{i}_l \\ \hat{i}_l = \sqrt{\hat{i}_{lI}^2 + \hat{i}_{lR}^2} \\ \hat{i}_{lI} = \hat{i}_{rI} - \hat{i}_{m2I} \\ \hat{i}_{lR} = \hat{i}_{rR} - \hat{i}_{m2R} \end{cases} \tag{13}$$

$$\begin{cases} x' = Ax + Bu \\ y = Cx + Du \end{cases} \tag{14}$$

By analyzing the sine and cosine circuits in Figure 7, it can be seen that there were nine state variables in the small-signal model, and the component corresponding to Lm1 had no effect on other parts. Therefore, similar to the small-signal model of the traditional unidirectional LLC resonant converter, it is a seventh-order system. The vector *x* of seven dimensions was derived by

$$x = \begin{bmatrix} \hat{i}_{rR} & \hat{i}_{rI} & \hat{v}_{cR} & \hat{v}_{cI} & \hat{i}_{m2R} & \hat{i}_{m2I} & \hat{v}_o \end{bmatrix}^T \tag{15}$$

The input vector and the output vector can be represented, respectively, by

$$\begin{cases} u = \hat{t}_s \\ y = \begin{bmatrix} \hat{v}_o & \hat{i}_{r\_avg} \end{bmatrix}^T \end{cases} \tag{16}$$

where $\hat{v}_o$ denotes the response of the output voltage, and $\hat{i}_{r\_avg}$ represents the response of the mean resonant current.

According to the definition for the average value of the resonant current, it can be obtained by

$$\hat{i}_{r\_avg} = \frac{2I_{rR}}{\pi\sqrt{I_{rR}^2 + I_{rI}^2}} \cdot \hat{i}_{rR} + \frac{2I_{rI}}{\pi\sqrt{I_{rR}^2 + I_{rI}^2}} \cdot \hat{i}_{rI} \tag{17}$$

where *IrI* and *IrR* are the imaginary and real components of *Ir* in the circuit, respectively.

From (12) to (17), coefficient matrices *A*, *B*, *C*, and *D* of the state equation were obtained as follows:

$$A = \begin{bmatrix} \frac{k_1}{L_r} & -2\pi f_s - \frac{k_2}{L_r} & -\frac{1}{L_r} & 0 & \frac{k_1}{L_r} & \frac{k_2}{L_r} & -\frac{k_3}{L_r} \\ 2\pi f_s - \frac{k_4}{L_r} & -\frac{k_5}{L_r} & 0 & -\frac{1}{L_r} & \frac{k_4}{L_r} & \frac{k_5}{L_r} & -\frac{k_6}{L_r} \\ \frac{1}{C_r} & 0 & 0 & -2\pi f_s & 0 & 0 & 0 \\ 0 & \frac{1}{C_r} & 2\pi f_s & 0 & 0 & 0 & 0 \\ \frac{k_1}{L_{m2}} & \frac{k_2}{L_{m2}} & 0 & 0 & -\frac{k_1}{L_{m2}} & -2\pi f_s - \frac{k_2}{L_{m2}} & \frac{k_3}{L_{m2}} \\ \frac{k_4}{L_{m2}} & \frac{k_5}{L_{m2}} & 0 & 0 & 2\pi f_s - \frac{k_4}{L_{m2}} & -\frac{k_5}{L_{m2}} & \frac{k_6}{L_{m2}} \\ \frac{c_1}{C_o} & \frac{c_2}{C_o} & 0 & 0 & -\frac{c_1}{C_o} & -\frac{c_2}{C_o} & \frac{1}{R_o C_o} \end{bmatrix}$$

$$B = -2\pi f_s^2 \cdot \begin{bmatrix} -I_{rI} & I_{rR} & -V_{cI} & V_{cR} & -I_{m2I} & I_{m2R} & 0 \end{bmatrix}^T,$$

$$C = \begin{bmatrix} C_v \\ C_i \end{bmatrix} = \begin{bmatrix} 0 & 0 & 0 & 0 & 0 & 1 \\ \frac{2I_{rR}}{\pi\sqrt{I_{rR}^2+I_{rI}^2}} & \frac{2I_{rI}}{\pi\sqrt{I_{rR}^2+I_{rI}^2}} & 0 & 0 & 0 & 0 & 0 \end{bmatrix},$$

$$D = \begin{bmatrix} 0 & 0 & 0 & 0 & 0 & 0 & 0 \\ 0 & 0 & 0 & 0 & 0 & 0 & 0 \end{bmatrix}.$$

Apply Laplace transform to (12) and (17):

$$\begin{cases} x = (sI - A)^{-1}Bu \\ y = C(sI - A)^{-1}Bu \end{cases} \tag{18}$$

Using (14), the transfer function *Gvt* was derived from the output voltage response and the input switching periodic interference amount; the transfer function *Git* was also obtained from the response of the resonant current average and the input switching periodic interference amount. The matrix consisting of *Gvt*, and *Git* was given by

$$\begin{bmatrix} G_{vt} \\ G_{it} \end{bmatrix} = C(sI - A)^{-1}B \tag{19}$$

The transfer function *Gvi* via the output voltage response and the average resonant current response was obtained by

$$G_{vi} = \frac{G_{vt}}{G_{it}} \tag{20}$$

3.3. Design of Control Loop

From (16) to (20), the program was written in MATLAB. Parameters were set as follows: *Vbus* = 400 V, *Vo* = 48 V, *T1* = 8.3:1, *Cr* = 188 nF, *Lr* = 20 µH, and *Lm1* = *Lm2* = 100 µH. Meanwhile, bode diagrams of the *Gvi*, *Gvt*, and *Git* were obtained by setting five switching frequencies, including 50 kHz, 65 kHz, 80 kHz, 120 kHz, and 160 kHz.

According to Figures 8 and 9, the dominant poles of the system transfer function *Gvt* and *Git* in the low-frequency band were consistent and could cancel each other, so it can be known that *Gvi* is a system with an order less than seven [32,33]. Based on the analysis of Figure 10, it can be seen that the system transfer function *Gvi* had good consistency under different fs, and the control strategy of the bidirectional LLC resonant converter was double-loop control, as shown in Figure 11.

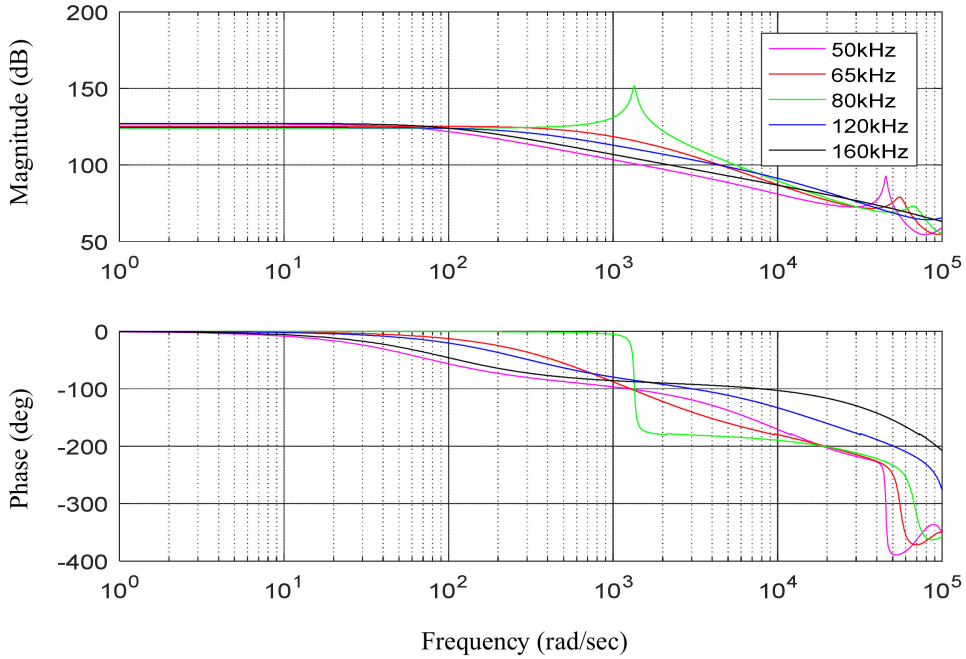

Figure 8. Bode diagram of system transfer function *Gvt*.

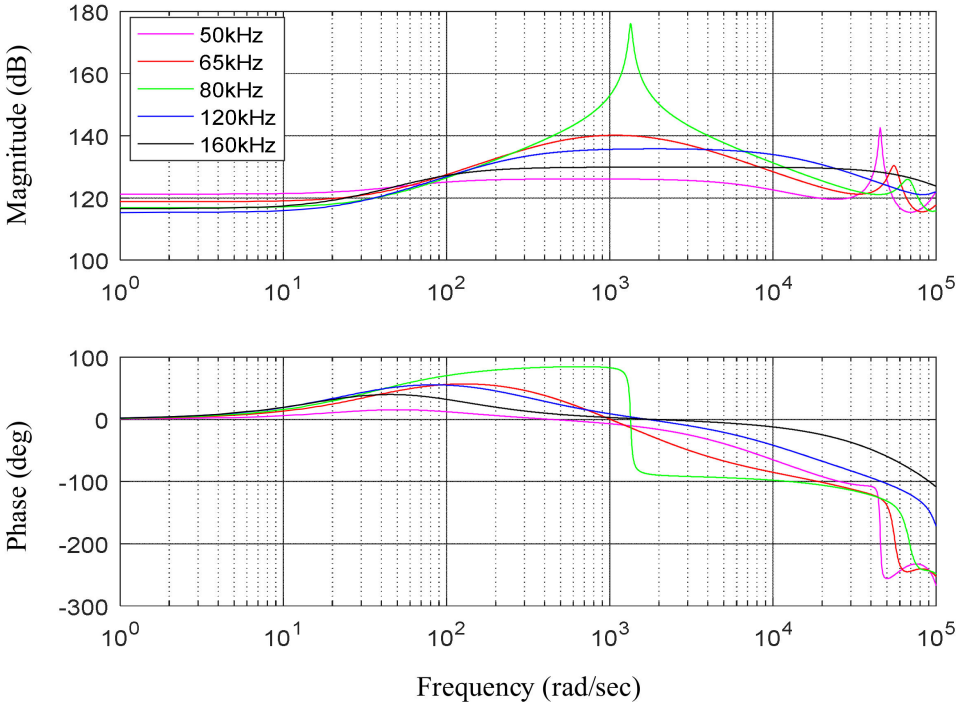

Figure 9. Bode diagram of system transfer function *Git*.

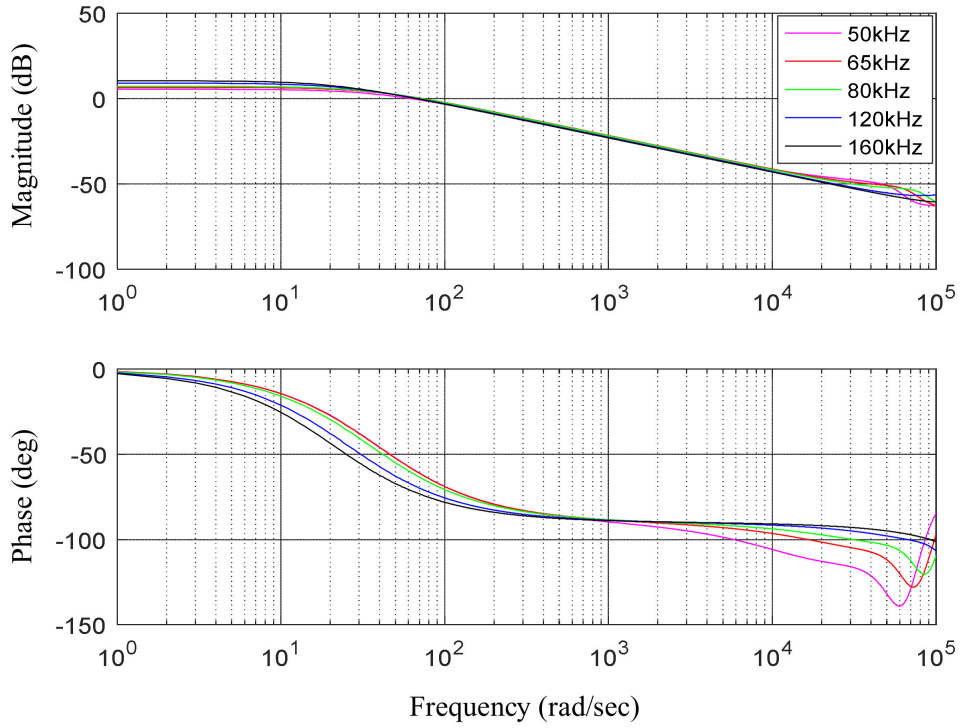

Figure 10. Bode diagram of system transfer function *Gvi*.

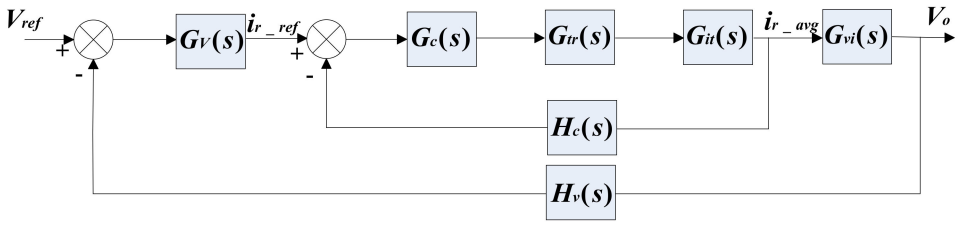

Figure 11. Double closed-loop control block diagram.

As can be seen from Figure 11, the outer voltage loop controls the output voltage *Vo*, and the inner current loop controls the average resonant current *ir_avg*.

4. Control Strategy of Energy Storage System

According to the above analysis, and combined with the operation principle of the energy storage system, when the energy of the system is sufficient, the bus charges the battery by the bidirectional LLC resonant converter, and the battery discharges while there is not enough energy in the system. Due to the symmetry of the bidirectional LLC resonant converter under the positive and negative operation conditions, the control loops under the two modes are the same, but the objects controlled are different. When the battery is charged, the objects controlled are the voltage and the current of the low-voltage side, and when the battery discharges, the object controlled is the voltage of the high-voltage side.

In the energy storage system, the energy control is coupled with the bus capacitor. To realize the energy dispatching of the small system, it is necessary to decouple the control of the bus voltage and optimize and design a reasonable control loop based on the actual voltage range.

Figure 12 shows the positive charging control block diagram of the bidirectional LLC resonant converter. It can be seen that *Vbat*, *Vbat_ref*, *Ibat*, *Ibat_ref*, and *iref* denote the sample value of battery voltage, setting value of battery voltage, sample value of battery

current, setting value of battery current, and the average value of the resonant current, respectively.

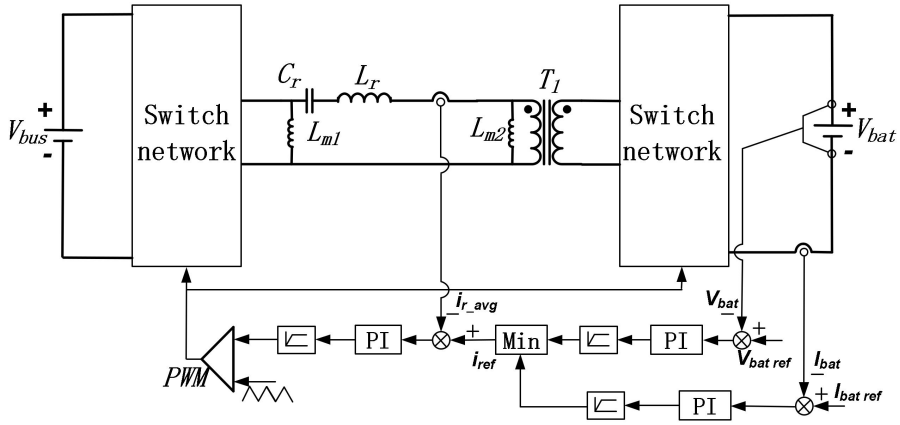

Figure 12. Control block diagram of the converter under the charging model.

As can be seen from the negative discharging control block diagram of the bidirectional LLC resonant converter in Figure 13, *Vbus*, *Vbus_ref*, and *ir_avg* represent the sample value of bus voltage, setting the value of bus voltage after decoupling, and the average value of resonant current, respectively. The output voltage under battery discharging is controlled by the command value of bus voltage.

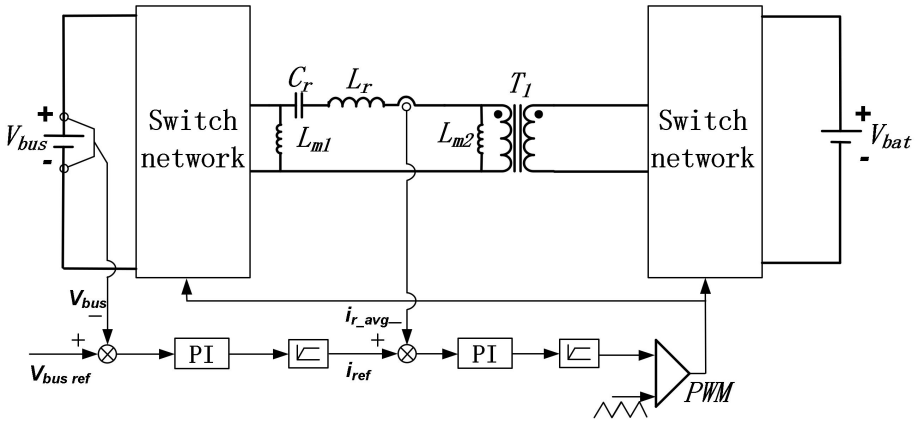

Figure 13. Control block diagram of the converter under discharging model.

5. Experimental Results

Given the above analysis, a 5 kW photovoltaic energy storage inverter was built, which included a 5 kW boost module, 3 kW bidirectional LLC resonant converter, and 3 kW DC/AC module. The parameters of the bidirectional LLC resonant converter refer to the parameters in Section 3.3, the operation range of the operation of battery voltage ranges from 42 V to 57 V, there is a capacity of 100 Ah in the battery pack, and the charging current is 25 A; the bus is between 350 V to 450 V. Experimental platform and control loop parameters are shown in Table 1.

Table 1. Experiment platform parameters and control-loop parameters.

Parameters	Name	Value
battery parameters	capacity voltage ranges	100 Ah 42 V to 57 V
LLC parameters	*T1* *Cr* *Lr* *Lm1* *Lm2* Rated Power	8.3:1 188 nF 20 μH 100 μH 100 μH 3 KW
DC/AC parameters	DC bus voltage ranges Rate AC Voltage Rated Power	350 V to 450 V. 220 V 3 KW
PV parameters	MPPT voltage ranges Rated Power	150 V~400 V 5 KW
Control parameters	Voltage loop Kp Voltage loop Ki Current loop Kp Current loop Ki	0.25 0.00015 0.05 0.0001

The experiment platform is shown in Figure 14. It includes the input and output analog source, load, and battery pack.

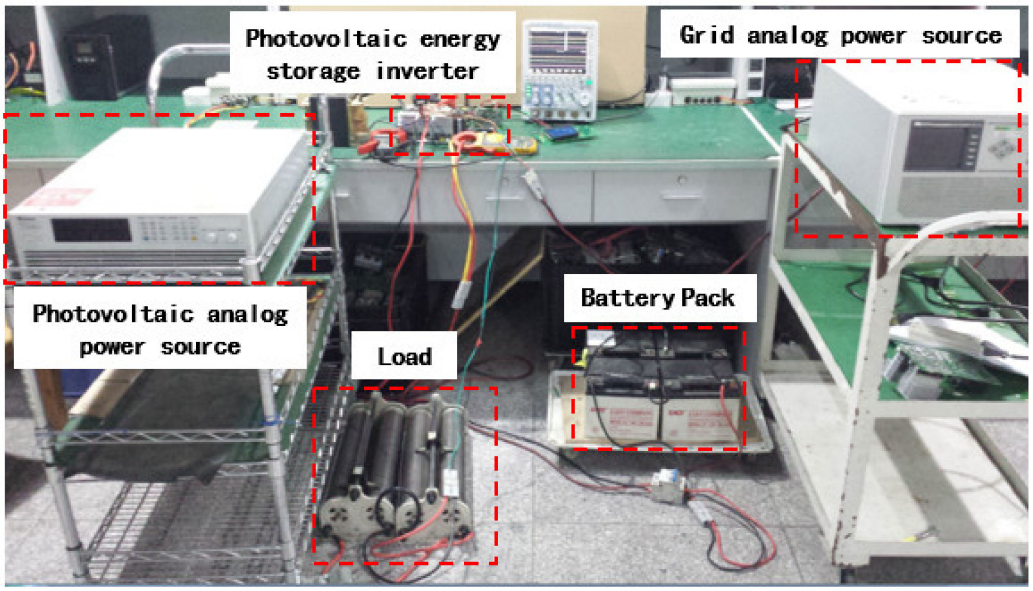

Figure 14. Experiment platform.

Soft-switching waveforms at different switching frequencies are shown in Figures 15–17, where *VLm1*, *Vin*, *ir*, *iLm1*, *id*, and *imos* represent the compensation inductor voltage, input voltage, resonant current, compensation inductor current, diode current, and low-voltage side MOS tube current of the bidirectional LLC resonant converter.

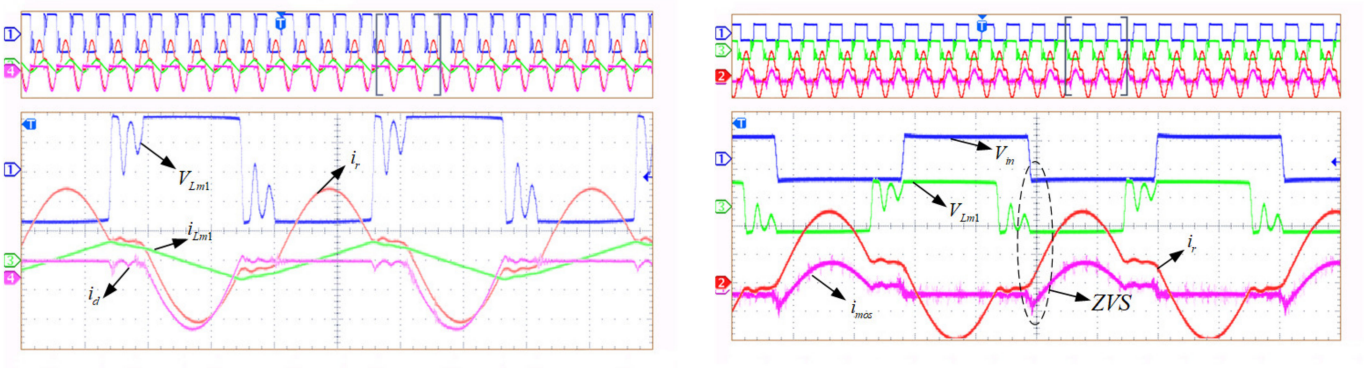

(**a**) (**b**)

Figure 15. Experimental waveform when switching frequency is less than the resonant frequency, and (**a**,**b**) show the corresponding current of the diode and low-voltage side MOS tube, respectively.

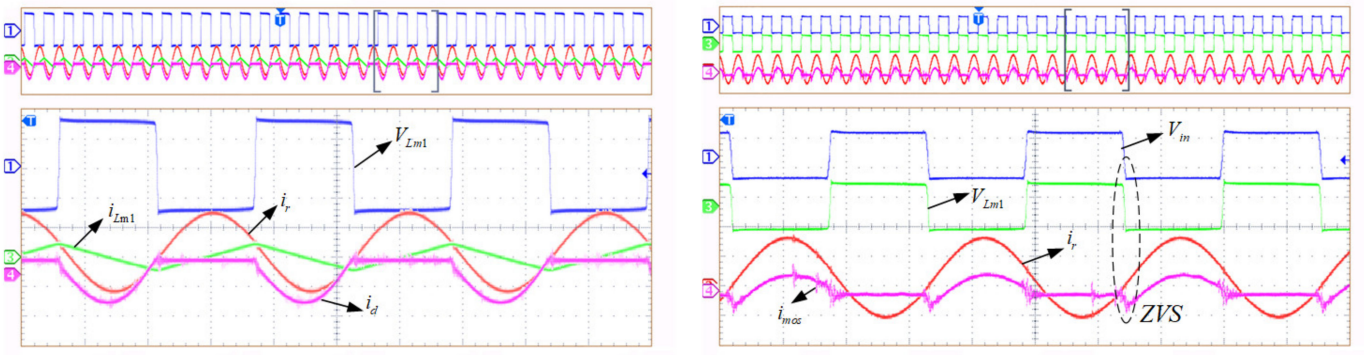

(**a**) (**b**)

Figure 16. Experimental waveforms at switching frequency equal to the resonant frequency, and (**a**,**b**) show the corresponding current of the diode and low-voltage side MOS tube, respectively.

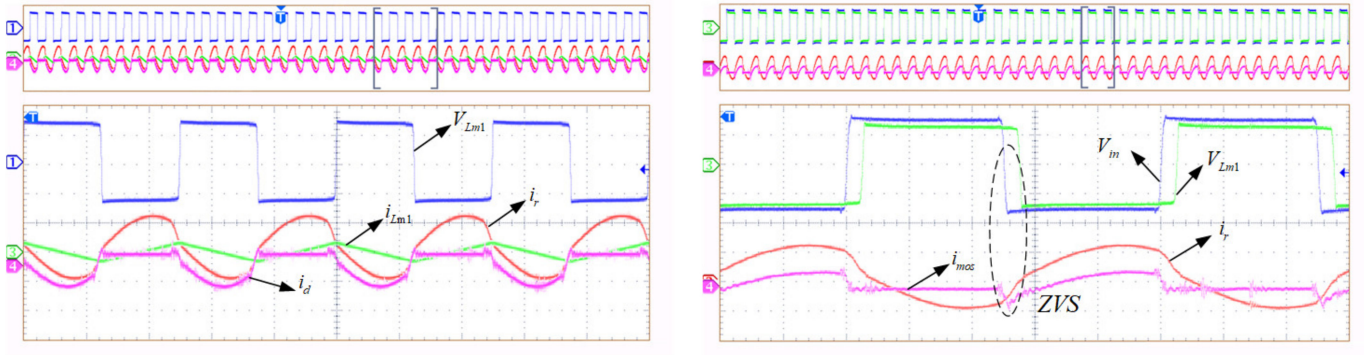

(**a**) (**b**)

Figure 17. Experimental waveform when switching frequency is greater than the resonant frequency, and (**a**,**b**) show the corresponding current of the diode and low-voltage side MOS tube, respectively.

Figure 15 shows the experimental waveform, where the switching frequency fs is 60 kHz, and the switching frequency fs of the converter is less than the resonant frequency fr. It can be seen from the experimental waveform that the converter was still in a continuous conduction state when the switching frequency was less than the resonant frequency; the experimental results are consistent with theoretical analysis.

Figure 16 shows the experimental waveform, where the switching frequency fs is 80 kHz, and the switching frequency fs of the converter is equal to the resonant frequency

fr. It can be seen from the experimental waveform that the switch tube at the input end can realize ZVS, and the switch tube at the output end can realize ZCS.

Figure 17 shows the experimental waveform, where the switching frequency fs is 100 kHz, and the switching frequency fs of the converter is greater than the resonant frequency fr. It can be seen from the experimental waveform that the input switch tube can still realize ZVS; the shut-off current of the output switch tube is greater than zero because the MOS tube fly-wheel diode recovery features are worse, so there is a shock.

The experimental results of charging and discharging are shown in Figures 18–20, where *Vbat*, *Vbus*, *Ibat*, and Iload represent battery voltage, bus voltage, battery current, and load current of the energy storage system. Figure 18a,b shows the charging waveform of the bidirectional LLC resonant converter at 350 V and 450 V bus voltage, respectively. Figure 19 shows the discharge waveform of the bidirectional LLC resonant converter; it can be seen that the switching of the output load of the energy storage system caused the fluctuation of the bus voltage. Figure 20 shows the experiment waveform of the bidirectional LLC resonant converter from charging to discharging; it can be known that there were abrupt changes in battery voltage and current, but stable operation of output load was not affected.

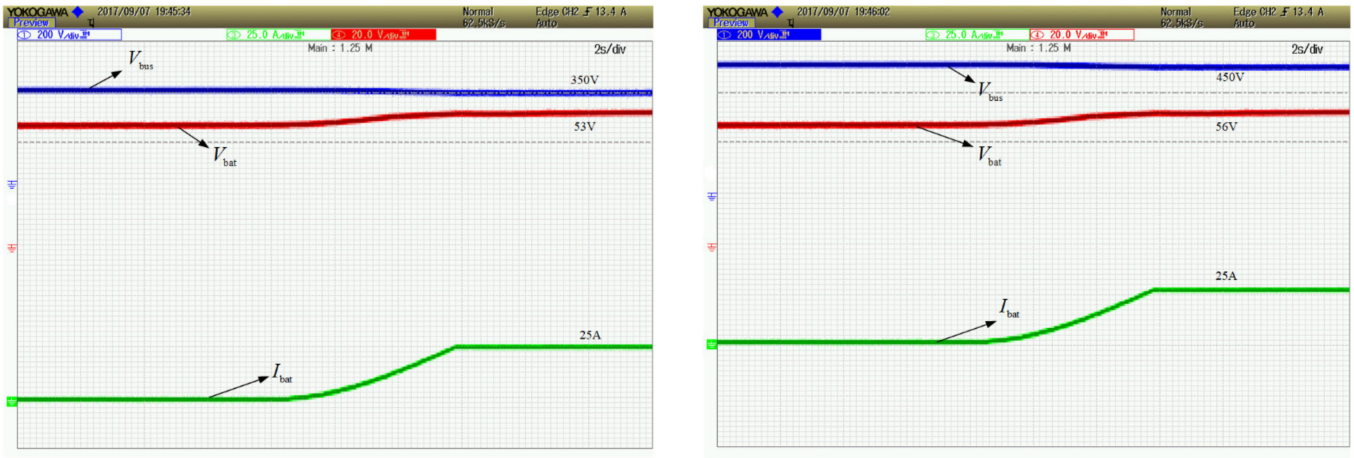

(**a**) (**b**)

Figure 18. The experiment waveform of the converter under different charging modes and the bus voltages in (**a**,**b**) are 350V and 450V, respectively.

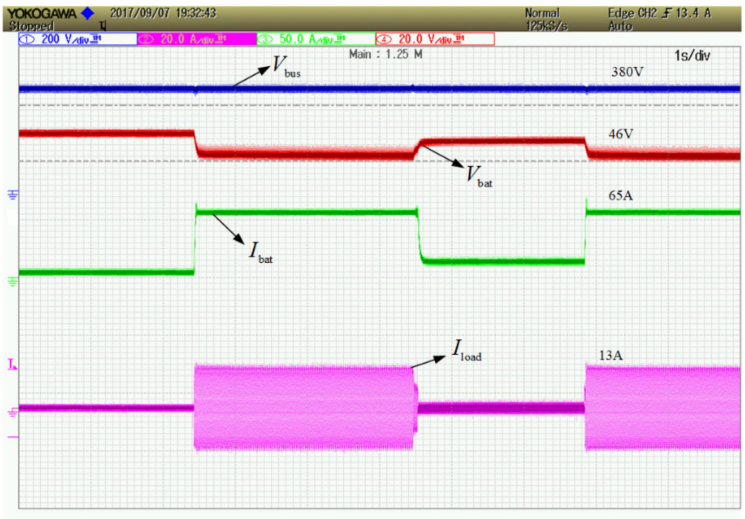

Figure 19. Experiment waveform of the converter under discharging mode.

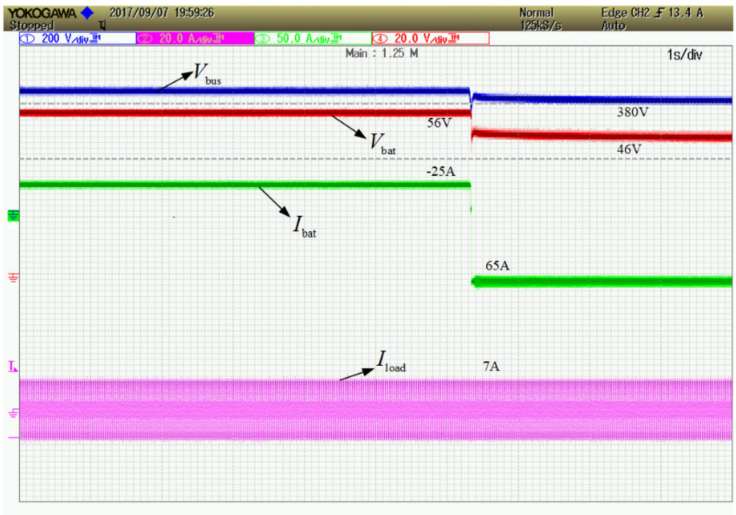

Figure 20. Experiment waveform of the converter from charging to discharging mode.

Figures 18 and 19 show that the bidirectional LLC resonant converter meets the charge and discharge requirements of the energy storage system. The voltage and current were smooth during the soft-start process, and the voltage adjustment characteristics of a wide range were met. When the load on the AC side of the energy storage system is switched suddenly, double closed-loop control of the LLC resonant converter can respond quickly, and the system goes into a stable state to ensure the stability of the output voltage on the high voltage side.

Figure 20 shows that the positive and negative control strategies of the bidirectional LLC resonant converter are designed reasonably. The switching speed is faster under the charging and discharging control strategy, and power balance can be achieved in the energy storage system.

At the same time, through the charging and discharging efficiency test of the energy storage system, the efficiency advantage of the bidirectional LLC resonant converter system is obvious, compared with that of the traditional, hard-switching DC converter system. The energy flow efficiency of the bidirectional LLC resonant converter system is improved by over 3%, which meets the high-efficiency requirements of the optical storage hybrid system. The working efficiency of the switch is compared with that of the traditional hard-switch control under different working conditions, as shown in Table 2.

Table 2. Efficiency comparison under different operation modes.

Project	Power Direction		
	Lithium Batteries Get Power from the PV	**Lithium Batteries Get Power from the Grid**	**Lithium Batteries Sends Power to the Grid**
Hard-Switch DC converter system efficiency	93.5%	92.6%	92.3%
The bidirectional LLC resonant converter system efficiency	96.9%	96.1%	95.6%

6. Conclusions

Because of the narrow input voltage range, low conversion efficiency, and the non-isolation of input and output voltage for the conventional bidirectional DC/DC converter, a novel bidirectional LLC resonant converter topology was proposed and applied to the photovoltaic energy storage complementary system in this paper. Theoretical analysis and experimental results demonstrated that the system has the following characteristics:

(1) Bidirectional symmetry of the converter can be achieved because of the addition of the compensating inductor. The converter has the advantage of simple control, and the soft-switching of the converter operating in both directions of power flow also can be achieved under the full-load range.
(2) By analyzing the operation principle of the LLC bi-directional DC/DC converter, the gain of the bidirectional operation of the converter is derived. The converter can operate with the switching frequency between 50 kHz and 160 kHz, and the voltage gain range is around 1.3 to 0.8, correspondingly. Finally, the demand for a wide range of actual output voltage is met, and the margin is sufficient.
(3) Compared with the system based on a conventional hard-switching DC/DC converter, there are more obvious advantages in the system based on a bidirectional LLC resonant converter. Improvement of efficiency of more than 3% for a bidirectional LLC resonant converter can be achieved in both directionals of power flow, which meets the high-efficiency requirements of the photovoltaic energy storage hybrid system.

Author Contributions: Conceptualization, D.X.; Formal analysis, D.X., Z.Z. and L.K.; Funding acquisition, S.W.; Investigation, J.Y.; Methodology, D.X.; Project administration, D.X.; Resources, S.W.; Software, L.W.; Supervision, D.X.; Validation, L.W.; Visualization, D.X.; Writing—original draft, L.W.; Writing—review & editing, D.X. All authors have read and agreed to the published version of the manuscript.

Funding: This research received no external funding.

Institutional Review Board Statement: Not applicable.

Informed Consent Statement: Not applicable.

Conflicts of Interest: Author Liangliang Wang, Shoumo Wang, and Jigang Yao are/were employed by Guangdong HYNN Technologies Co., Ltd. The remaining authors declare that the research was conducted in the absence of any commercial or financial relationships that could be construed as a potential conflict of interest.

References

1. Li, R.; Shi, F. Control and Optimization of Residential Photovoltaic Power Generation System with High Efficiency Isolated Bidirectional DC-DC Converter. *IEEE Access* **2019**, *7*, 116107–116122. [CrossRef]
2. Gorji, S.A.; Sahebi, H.G.; Ektesabi, M.; Rad, A.B. Topologies and Control Schemes of Bidirectional DC-DC Power Converters: An Overview. *IEEE Access* **2019**, *7*, 117997–118019. [CrossRef]
3. Inoue, S.; Ishigaki, M.; Takahashi, A.; Sugiyama, T. Design of an Isolated Bidirectional DC-DC Converter with Built-in Filters for High Power Density. *IEEE Trans. Power Electron.* **2021**, *36*, 739–750. [CrossRef]
4. Zhang, N.; Sutanto, D.; Muttaqi, K.M. A four-port DC-DC converter to integrate energy storage system and solar PV to supply the grid and local load demand. In Proceedings of the Australasian Universities Power Engineering Conference (AUPEC), Wollongong, NSW, Australia, 27–30 September 2015; pp. 1–6. [CrossRef]
5. Ning, J.; Zeng, J.; Du, X. A Four-Port Bidirectional DC-DC Converter for Renewable Energy-Battery-DC Microgrid System. In Proceedings of the IEEE Energy Conversion Congress and Exposition (ECCE), Baltimore, MD, USA, 29 September–3 October 2019; pp. 6722–6727. [CrossRef]
6. Chen, C.; Zhao, X.; Yeh, C.; Lai, J. Analysis of the Zero-Voltage Switching Condition in LLC Series Resonant Converter with Secondary Parasitic Capacitors. In Proceedings of the IEEE Applied Power Electronics Conference and Exposition (APEC), Anaheim, CA, USA, 17–21 March 2019; pp. 828–832. [CrossRef]
7. Zhou, J.; Ma, H. Full-Bridge LLC Resonant Converter with Parallel-Series Transformer Connection and Voltage Doubler Rectifier. In Proceedings of the 2019 10th International Conference on Power Electronics and ECCE Asia (ICPE 2019—ECCE Asia), Busan, Korea, 27–31 May 2019; pp. 1–6. [CrossRef]
8. Wei, Y.; Mantooth, A. Topology Morphing Control Strategies for Full-bridge LLC Converter. In Proceedings of the 5th IEEE Workshop on the Electronic Grid (eGRID), Aachen, Germany, 2–4 November 2020; pp. 1–5. [CrossRef]
9. Zhu, A.; Ma, Y.; Liu, Z.; Lu, H.; Zhang, F. Optimal Design of Control Strategy for Full-Bridge LLC Converter. In Proceedings of the IEEE Energy Conversion Congress and Exposition (ECCE), Detroit, MI, USA, 11–15 October 2020; pp. 2251–2257. [CrossRef]
10. Lu, J.; Wang, Y.; Li, X.; Du, C. High-Conversion-Ratio Isolated Bidirectional DC-DC Converter for Distributed Energy Storage Systems. *IEEE Trans. Power Electron.* **2019**, *34*, 7256–7277. [CrossRef]
11. Shi, L.; Liu, B.; Duan, S. Burst-Mode and Phase-Shift Hybrid Control Method of LLC Converters for Wide Output Range Applications. *IEEE Trans. Ind. Electron.* **2020**, *67*, 1013–1023. [CrossRef]

12. Zhang, J.; Liu, J.; Yang, J.; Zhao, N.; Wang, Y.; Zheng, T.Q. An LLC-LC Type Bidirectional Control Strategy for an LLC Resonant Converter in Power Electronic Traction Transformer. *IEEE Trans. Power Electron.* **2018**, *65*, 8595–8604. [CrossRef]
13. Kim, J.W.; Lee, M.; Lai, J.S. Efficient LLC resonant converter with a simple hold-up time compensation in voltage doubler rectifier. *IEEE J. Emerg. Sel. Top. Power Electron.* **2019**, *7*, 843–850. [CrossRef]
14. He, P.; Mallik, A.; Cooke, G.; Khaligh, A. High-power-density high-efficiency LLC converter with an adjustable-leakage-inductance planar transformer for data centers. *IET Power Electron.* **2019**, *12*, 303–310. [CrossRef]
15. Li, Y.; Shao, S.; Chen, H.; Zhang, J.; Sheng, K. High-gain high-efficiency IPOS LLC converter with coupled transformer and current sharing capability. *CPSS Trans. Power Electron. Appl.* **2020**, *5*, 63–73. [CrossRef]
16. Wang, C.-S.; Zhang, S.-H.; Wang, Y.-F.; Chen, B.; Liu, J.-H. A 5-kW Isolated High Voltage Conversion Ratio Bidirectional CLTC Resonant DC-DC Converter with Wide Gain Range and High Efficiency. *IEEE Trans. Power Electron.* **2019**, *34*, 340–355. [CrossRef]
17. Blinov, A.; Kosenko, R.; Chub, A.; Vinnikov, D. Bidirectional Soft Switching Current Source DC-DC Converter for Residential DC Microgrids. In Proceedings of the IECON 2018—44th Annual Conference of the IEEE Industrial Electronics Society, Washington, DC, USA, 21–23 October 2018; pp. 6059–6064. [CrossRef]
18. Mukherjee, S.; Mukherjee, D.; Kastha, D. Multiport Soft-Switching Bidirectional DC-DC Converter for Hybrid Energy Storage Systems. In Proceedings of the IEEE Applied Power Electronics Conference and Exposition (APEC), Anaheim, CA, USA, 17–21 March 2019; pp. 2103–2109. [CrossRef]
19. Jean-Pierre, G.; el Shafei, A.; Altin, N.; Nasiri, A. A Multiport Bidirectional LLC Resonant Converter for Grid-Tied Photovoltaic-Battery Hybrid System. In Proceedings of the 8th International Conference on Renewable Energy Research and Applications (ICRERA), Brasov, Romania, 3–6 November 2019; pp. 755–760. [CrossRef]
20. Jean-Pierre, G.; Altin, N.; Nasiri, A. A Three-Port LLC Resonant Converter for Photovoltaic-Battery Hybrid System. In Proceedings of the IEEE Transportation Electrification Conference and Expo (ITEC), Detroit, MI, USA, 8 August 2019; pp. 1–6. [CrossRef]
21. Parida, A.; Barai, M.; Mothukuri, K.R. Study of a soft switched Isolated DC-DC Bidirectional Converter for Electric Vehicles. In Proceedings of the TENCON 2019—2019 IEEE Region 10 Conference (TENCON), Kochi, India, 17–20 October 2019; pp. 1136–1141. [CrossRef]
22. Vuchev, A.S.; Bankov, N.D.; Lichev, A.A. A control technique for a bidirectional series resonant DC-DC converter. In Proceedings of the XXVI International Scientific Conference Electronics (ET), Sozopol, Bulgaria, 13–15 September 2017; pp. 1–4. [CrossRef]
23. Lichev, A.A.; Vuchev, A.S. Bidirectional Series Resonant DC-DC Converter Performance Improvement. In Proceedings of the XI National Conference with International Participation (ELECTRONICA), Sofia, Bulgaria, 23–24 July 2020; pp. 1–4. [CrossRef]
24. Bhajana, V.V.S.K.; Drabek, P. A Novel ZCS/ZVS Bidirectional DC-DC Converter for Energy Storage Applications. In Proceedings of the International Conference on Applied Electronics (AE), Pilsen, Czech Republic, 10–11 September 2019; pp. 1–6. [CrossRef]
25. Babu, B.; Divya, S. A Novel soft switching bidirectional dc dc converter. In Proceedings of the Second International Conference on Inventive Communication and Computational Technologies (ICICCT), Coimbatore, India, 20–21 April 2018; pp. 1752–1756. [CrossRef]
26. Yanna, V.S.R.; Bhajana, V.V.S.K.; Drabek, P.; Popuri, M. A Novel Soft-Switching Bidirectional DC-DC Converter for Energy Storage Applications. In Proceedings of the International Conference on Applied Electronics (AE), Pilsen, Czech Republic, 8–9 September 2020; pp. 1–4. [CrossRef]
27. Kim, E.; Oh, J.; Kim, M.; Lee, J.; Woo, J.; Jeon, Y. Enhancing Efficiency in Bidirectional Resonant DC-DC Converter. In Proceedings of the IEEE Applied Power Electronics Conference and Exposition (APEC), New Orleans, LA, USA, 15–19 March 2020; pp. 2230–2235. [CrossRef]
28. Hsieh, Y.; Lee, F.C. Accurate Small-Signal Model for LLC Resonant Converters. In Proceedings of the IEEE Energy Conversion Congress and Exposition (ECCE), Baltimore, MD, USA, 29 September–3 October 2019; pp. 660–665. [CrossRef]
29. Zong, S.; Luo, H.; Li, W.; He, X.; Xia, C. Theoretical Evaluation of Stability Improvement Brought by Resonant Current Loop for Paralleled LLC Converters. *IEEE Trans. Ind. Electron.* **2015**, *62*, 4170–4180. [CrossRef]
30. Murakami, Y.; Sato, T.; Nishijima, K.; Nabeshima, T. Small signal analysis of LLC current resonant converters using equivalent source model. In Proceedings of the IECON 2016—42nd Annual Conference of the IEEE Industrial Electronics Society, Florence, Italy, 23–26 October 2016; pp. 1417–1422. [CrossRef]
31. Cittanti, D.; Gregorio, M.; Armando, E.; Bojoi, R. Digital Multi-Loop Control of an LLC Resonant Converter for Electric Vehicle DC Fast Charging. In Proceedings of the IEEE Energy Conversion Congress and Exposition (ECCE), Detroit, MI, USA, 11–15 October 2020; pp. 4423–4430. [CrossRef]
32. Huang, Y.; Hsieh, Y.; Lin, Y.; Chiu, H.; Lin, J. Study and Implementation on Start-Up Control of Full-Bridge LLC Resonant Converter. In Proceedings of the IEEE Transportation Electrification Conference and Expo, Asia-Pacific (ITEC Asia-Pacific), Bangkok, Thailand, 6–9 June 2018; pp. 1–5. [CrossRef]
33. Hsieh, Y.-H.; Lee, F.C. Small-Signal Dynamic and High-Bandwidth Design of LLC Resonant Converters. In Proceedings of the IEEE Energy Conversion Congress and Exposition (ECCE), Detroit, MI, USA, 11–15 October 2020; pp. 6136–6143. [CrossRef]